Surface-Induced Liquid Crystal Transitions of Wormlike Polymers Confined in a Narrow Slit. A Mean-Field Theory

Jeff Z. Y. Chen,*,† D. E. Sullivan,‡ and Xiangqun Yuan†

Guelph−Waterloo Physics Institute and Department of Physics and Astronomy, University of Waterloo, Waterloo, Ontario, Canada N2L 3G1, and Guelph−Waterloo Physics Institute and Department of Physics, University of Guelph, Guelph, Ontario, Canada N1G 2W1

Received September 18, 2006; Revised Manuscript Received November 20, 2006

ABSTRACT: On the basis of a mean-field treatment of semiflexible polymer chains, we analyze the structure of long wormlike polymers sterically confined between two parallel, structureless walls separated by a distance *W*. With the Onsager excluded-volume interaction between polymer segments, the system displays three phases, uniaxial, biaxial, and condensed, depending on the polymer density and *W*. We have also determined the induced attractive force acting on the walls, mediated by the Onsager excluded-volume interaction between polymer segments.

I. Introduction

Khokhlov and Semenov[1] extended the Onsager theory[2] for the isotropic−nematic phase transition of lyotropic rigid rods to solutions of semiflexible polymer chains. In such a lyotropic system, where the excluded-volume interaction between polymer segments dominates, the isotopic-nematic phase transition is completely driven by the segmental concentration of polymers.[3] According to the Khokhlov−Semenov theory, for long polymers (having a total backbone contour length L much greater than the persistence length l_p), the system undergoes a first-order phase transition when the reduced segmental density $\tilde{\rho}_b$ goes beyond an estimated value $\tilde{\rho}_I = 13.05$. Here $\tilde{\rho}_b = a^2 D \rho_b$, where ρ_b is the number of polymer segments (each having an effective Kuhn length $a = 2l_p$) per unit volume and D represents the excluded-volume diameter.[1,4−6] Other theoretical approaches to the problem have qualitatively given rise to a similar physical picture.[7−10] Indeed, experimentally, the isotropic−nematic transition has been observed in various physical systems to which these wormlike−polymer models can be applied.[11−19] As well, computer simulations have also confirmed the existence of this phase transition in a few models of the same nature.[20−23]

Near a *single* flat surface, Landau−de Gennes theories of thermotropic liquid crystals consisting of rigid molecules have been shown to produce several surface structures displaying different orientational and wetting properties.[24−27] Extending the Khokholov−Semenov theory of long wormlike polymers[28] to spatially inhomogeneous systems, Chen and Cui demonstrated that surface phases and phase transitions, with similar orientational structures to those of thermotropic systems, also exist in lyotropic liquid-crystalline polymer solutions near a single surface.[29] The surface structures of lyotropic systems (described below) turn out to be common for liquid-crystal solutions, regardless of whether they are composed of wormlike chains[29] or rigid rodlike molecules.[30−32]

In the current work, we focus on the physical properties of wormlike polymers confined between *two* flat surfaces separated by a distance *W*. An idealized example setup is an experiment where two structureless slabs of material, separated by a distance *W* and with flat surfaces of dimension much larger than *W*, are immersed in such a wormlike polymer solution (see Figure 1). As will be shown in section II, the physical properties depend on two reduced variables, W/a and $\beta\mu$, where μ is the segmental chemical potential, which can be related to the bulk segmental density ρ_b in the solution by $\beta\mu = (\pi/2)\tilde{\rho}_b$ in the bulk isotropic phase. Here $\beta = 1/k_B T$ with k_B the Boltzmann constant and T the temperature of the system. Depending on the magnitude of these variables, the system can display three different types of orientational phases (uniaxial, biaxial, or condensed) separated by first-order phase boundaries in most of the parameter regime, as shown in the phase diagram in Figure 2. This phase diagram shares many similarities with the phase diagram for lyotropic rigid rods in a slit, where a should be understood as the rod length, which has recently been derived by van Roij, Dijkstra, and Evans[30−32] based on an extension of the Zwanzig model.[33] In contrast with the present work, they have found that the uniaxial-biaxial transition is second-order and independent of W/a, possibly a consequence of the discrete-orientation nature of the Zwanzig model.

From calculation of the free energy of the wormlike polymer solution, in section III C, we demonstrate that the two slabs in Figure 1 experience a mutual attraction in all three phases, induced by the Onsager-type repulsion between polymer segments. Across the first-order phase boundaries, there is an abrupt change of the force acting on the slabs, which can be experimentally used as a signal in probing the phase boundaries.

II. Mean-Field Treatment

In this section, we present the theoretical approach used in finding the physical results described in the next section. Readers who are not interested in the technical details may directly proceed to the next section.

A. Onsager Approximation for the Mean Field. To include excluded-volume interactions, a wormlike chain can be treated as a cylindrical filament, characterized by a cross-sectional diameter D. We define $\rho(x,\mathbf{u})$ as the segmental distribution function averaged over the entire chain, i.e., the probability of finding a segment of the polymer to be located at x and with a tangent vector in direction $\mathbf{u}$. In a typical self-consistent mean-field approach for polymers, we introduce a mean-field potential

† Guelph−Waterloo Physics Institute and Department of Physics and Astronomy, University of Waterloo.

‡ Guelph−Waterloo Physics Institute and Department of Physics, University of Guelph.

10.1021/ma062160m CCC: $37.00
Published on Web 01/30/2007

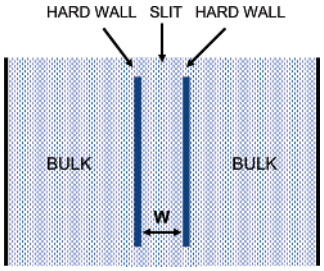

Figure 1. Idealized experimental setup that can be used to measure some of the physical properties predicted by the current work. A slit formed by two parallel plates is immersed in a solution of wormlike polymers, where the interior part of the solution between the plates is in equilibrium with the bulk phase.

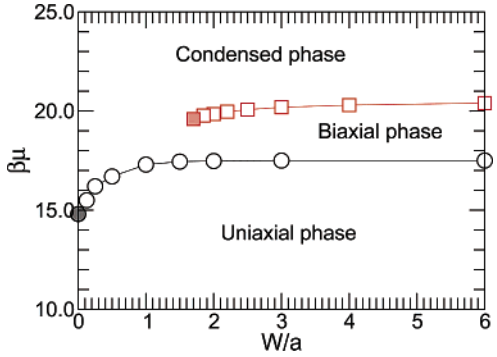

Figure 2. Phase diagram for wormlike chains confined between walls separated by distance W, in terms of the reduced chemical potential $\beta\mu$ per effective Kuhn segment. Open symbols represent the numerical solutions to the mean-field theory of this work, based on which solid curves (first-order phase boundaries) are projected. Filled symbols represent critical points.

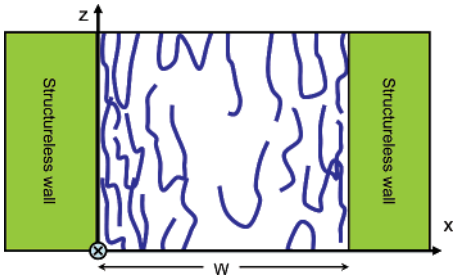

Figure 3. Schematic diagram of wormlike chains between two parallel walls and the coordinate system used.

$w(x,\mathbf{u})$ acting on a unit segment of the polymer chain. In the limit of $L \gg a$, we can approximate the grand free energy Ω of the entire system, as a functional of the undetermined density function, $\rho(x,\mathbf{u})$, by[1,28]

$$\beta\Omega/A = \beta\int_0^W dx d\mathbf{u}[V_W(x,\mathbf{u}) - w(x,\mathbf{u}) - \mu]\rho(x,\mathbf{u}) + a^2D\int_0^W dx \int d\mathbf{u}d\mathbf{u}'\,\rho(x,\mathbf{u})\rho(x,\mathbf{u}')|\mathbf{u}\times\mathbf{u}'| \quad (1)$$

where μ is the chemical potential and A is the area of the surface of the walls in Figure 3. In this expression, we have explicitly introduced an external wall potential, $V_w(x,\mathbf{u})$, that has a value of 0 for the region within the slit and ∞ outside the slit. The last term in this expression is based on the Onsager second-virial approximation for the excluded-volume interaction between two rods[2] pointing in directions specified by the unit vectors $\mathbf{u}$ and $\mathbf{u}'$. This approximation is considered accurate for long polymers,[1] where $L \gg a \gg D$, a condition that can be easily satisfied by most polymer systems, in particular, DNA molecules.

Minimizing the free energy Ω with respect to $\rho(x,\mathbf{u})$ yields an expression for the mean field

$$w(x,\mathbf{u}) = V(x,\mathbf{u}) - \mu \quad (2)$$

with

$$\beta V(x,\mathbf{u}) = 2a^2D\int d\mathbf{u}'\rho(x,\mathbf{u}')|\mathbf{u}\times\mathbf{u}'| + \beta V_w(x,\mathbf{u}) \quad (3)$$

where the first term on the right-hand side is the mean-field potential energy acting on a polymer segment due to other segments.

We are interested in the conditional probability, $\Psi(x,\mathbf{u};t)$, that a polymer portion of length t has an end located at x *and* whose tangent vector points in the direction $\mathbf{u}$, under such a potential energy. In the long polymer limit, $L \gg a$, one can show that $\Psi(x,\mathbf{u};t)$ satisfies the differential equation[34]

$$-\beta\mu\Psi_0(x,\mathbf{u}) = \left[\nabla_u^2 - au_x\frac{\partial}{\partial x} - \beta V(x,\mathbf{u})\right]\Psi_0(x,\mathbf{u}) \quad (4)$$

where u_x is the projection of $\mathbf{u}$ onto the x axis and

$$\Psi(x,\mathbf{u};t) \approx \Psi_0(x,\mathbf{u})\exp(-\beta\mu t) \quad (t \gg 1) \quad (5)$$

The function $\Psi_0(x,\mathbf{u})$ is connected to the segmental density $\rho(x,\mathbf{u})$ by

$$\rho(x,\mathbf{u}) = \Psi_0(x,\mathbf{u})\Psi_0(x,-\mathbf{u}) \quad (6)$$

The solution of the above partial differential equation for $\Psi_0(x,\mathbf{u})$ contains an undetermined coefficient, which can be pinned down by this connection, where $A\int dx \int d\mathbf{u}\,\rho(x,\mathbf{u})$ is the total number of polymer segments in the system. In the case of $D = 0$, when $V(x,\mathbf{u})$ is the wall confinement potential $V_w(x,\mathbf{u})$ only, the free energy of a wormlike chain has been calculated as a function of the confinement width W,[35] approaching scaling behaviors in the large-W/a[36,37] and small-W/a[38,39] limits, which can be both treated exactly.

With the introduction of the reduced coordinate

$$\tilde{x} \equiv x/a \quad (7)$$

and the reduced density

$$\tilde{\rho}(\tilde{x},\mathbf{u}) \equiv a^2D\rho(x,\mathbf{u}) \quad (8)$$

we can rewrite eq 3 as

$$\beta V(\tilde{x},\mathbf{u}) = 2\int d\mathbf{u}'\,\tilde{\rho}(\tilde{x},\mathbf{u}')|\mathbf{u}\times\mathbf{u}'| + \beta V_w(x,\mathbf{u}) \quad (9)$$

and eq 6 as

$$\tilde{\rho}(\tilde{x},\mathbf{u}) \equiv \tilde{\Psi}_0(\tilde{x},\mathbf{u})\tilde{\Psi}_0(\tilde{x},-\mathbf{u}) \quad (10)$$

where $\tilde{\Psi}_0(\tilde{x},\mathbf{u}) \equiv a\sqrt{D}\Psi_0(x,\mathbf{u})$. Substituting the last two equations into eq 4, we obtain a nonlinear integro-differential equation that determines the function $\Psi_0(\tilde{x},\mathbf{u})$ for given $\beta\mu$ and W/a. We solved the structure of interacting wormlike polymers through these equations by iteration. We assumed an initial guess for $\tilde{\Psi}_0(\tilde{x},\mathbf{u})$, solved the nonlinear integro-partial differential equation in eq 4 and then used the solution as the next guess for $\tilde{\Psi}_0(\tilde{x},\mathbf{u})$. The procedure was repeated until the solution converged.

With the usage of W/a and $\beta\mu$ as independent parameters, the surface tension between the two walls, σ, can be defined as the free energy of maintaining the density profile within the slit, relative to that of a bulk phase having the same value of $\beta\mu$. In the reduced version

$$\tilde{\sigma}(W/a,\beta\mu) \equiv aD\beta\sigma = \int_0^{W/a} d\tilde{x} \int d\mathbf{u}d\mathbf{u}'[\tilde{\rho}_b(\mathbf{u})\tilde{\rho}_b(\mathbf{u}') - \tilde{\rho}(\tilde{x},\mathbf{u})\tilde{\rho}(\tilde{x},\mathbf{u}')]|\mathbf{u}\times\mathbf{u}'| \quad (11)$$

where $\tilde{\rho}_b(\mathbf{u})$ is the segemental orientational distribution function of the bulk phase. In most parameter regimes discussed below, the bulk system is still in its isotropic phase, and we have[1,5,6]

$$\tilde{\rho}_b(\mathbf{u}) = \frac{\tilde{\rho}_b}{4\pi} = \frac{\beta\mu}{2\pi^2} \quad (12)$$

The formalism in this section follows those given in earlier work.[28,29] The published versions of these earlier work contained an extra factor of 2 in front of the Onsager term, a mistake introduced during the preparation of the manuscripts. On the other hand, the computational code was based on the correct version of the free energy; hence, the numerical results in these work are still valid.

B. Numerical Method. The variables in the integro-differential equation based on eqs 4 and 9 are $\tilde{x}$ and $\mathbf{u}$. In the actual numerical approach, we treated the $\mathbf{u}$ dependence of all functions involved using spherical-harmonic series and the $\tilde{x}$ dependence by means of direct discretization.

The reduced density function, $\tilde{\rho}(\tilde{x},\mathbf{u})$, for example, is represented by

$$\tilde{\rho}(\tilde{x},\mathbf{u}) = \sum_{l=0}^{\infty}\sum_{m=-l}^{l}\rho_{l,m}(\tilde{x})Y_{l,m}(\theta,\phi) \quad (13)$$

where the functions $\rho_{l,m}(\tilde{x})$ are dimensionless, to be determined numerically. The direction specified by the unit vector $\mathbf{u}$ is represented by the polar angle θ measured with respect to the z-axis and the azimuthal angle ϕ with respect to the x-axis (see Figure 3). Similarly, we write

$$\tilde{\Psi}_0(\tilde{x},\mathbf{u}) = \sum_{l=0}^{\infty}\sum_{m=-l}^{l}\Phi_{l,m}(\tilde{x})Y_{l,m}(\theta,\phi) \quad (14)$$

where the functions $\Phi_{l,m}(\tilde{x})$ and $\rho_{l,m}(\tilde{x})$ are connected by

$$\rho_{l,m}(\tilde{x}) = \sum_{l_1,m_1}\sum_{l_2,m_2} I_{l,-m,l_1,m_1,l_2,m_2}(-1)^{l_1+m}\Phi_{l_1,m_1}(\tilde{x})\Phi_{l_2,m_2}(\tilde{x}) \quad (15)$$

and where the definition of the coefficients I is given in Appendix A. The spherical-harmonic expansion for the kernel $|\mathbf{u}\times\mathbf{u}'|$ can be obtained by using the addition theorem[5]

$$|\mathbf{u}\times\mathbf{u}'| = \sum_{l=0}^{\infty}\sum_{m=-l}^{l}\frac{4\pi}{2l+1}d_l Y_{l,m}(\theta,\phi)Y^*_{l,m}(\theta',\phi') \quad (16)$$

where the coefficients d_l ($l = 0, 1, ...$) can also be found in Appendix A, and θ' and ϕ' are the spherical angles used to specify the unit vector $\mathbf{u}'$. Finally, the external potential function $V_w(x,\mathbf{u})$ depends on both orientation and position, even for a square well potential, and must be treated carefully.[29,35,39] A spherical-harmonic expansion can be obtained based on the step function boundary condition in our earlier publications[29,35]

$$\beta V_w(x,\mathbf{u}) = \sum_{l=0}^{\infty}\sum_{m=-l}^{l}v_{l,m}(x)Y_{l,m}(\theta,\phi) \quad (17)$$

With these definitions, we can rewrite eq 4 as

$$[l(l+1)-\beta\mu]\Phi_{l,m}(\tilde{x}) + (-1)^m\sum_{l_1,l_2,m_1,m_2} I_{l,-m,l_1,m_1,l_2,m_2}v_{l_1,m_1}(\tilde{x})\Phi_{l_2,m_2}(\tilde{x}) + (-1)^m\sqrt{\frac{2\pi}{3}}\sum_{l_1,m_1}(I_{1,-1,l_1,m_1,l,-m} - I_{1,1,l_1,m_1,l,-m})\frac{d\Phi_{l_1,m_1}(\tilde{x})}{d\tilde{x}} + \sum\frac{8\pi}{2l_1+1}(-1)^{l_4+m+m_1}d_{l_1}\Phi_{l_2,m_2}(\tilde{x})\Phi_{l_3,m_3}(\tilde{x})\Phi_{l_4,m_4}(\tilde{x})I_{l,-m,l_1,m_1,l_2,m_2}I_{l_1,-m_1,l_3,m_3,l_4,m_4} = 0 \quad (18)$$

where the last summation is over eight indices (l_1,l_2,l_3,l_4,m_1,m_2, m_3,m_4). The numerical challenge becomes solving the coupled differential equations of the above form for $\Phi_{l,m}(\tilde{x})$ where $l = 0, 1, 2, 3, ...$ and $m = -l, -l+1, ..., l-1, l$. Using these spherical-harmonic expansions, we can rewrite the surface tension defined in eq 11 as

$$\tilde{\sigma} = \frac{W}{a}\frac{(\beta\mu)^2}{\pi} - 4\pi\int_0^{W/a}d\tilde{x}\left[\sum_{l,m}\frac{(-1)^m d_{2l}\rho_{2l,m}(\tilde{x})\rho_{2l,-m}(\tilde{x})}{4l+1}\right] \quad (19)$$

when the reference bulk system is in its isotropic phase.

In our calculations, we have truncated the infinite sums over l by finite sums over the range $l = 0, 1, 2, ..., l_{max}$. We have also introduced N_x divisions to divide the space $[0,W/a]$ for $\tilde{x}$ into $N_x + 1$ nodes on which the function $\Phi_{l,m}(\tilde{x})$ is represented. The derivative term, $d\Phi_{l,m}(\tilde{x})/d\tilde{x}$, was then represented by a central difference, except for the two boundary points at $\tilde{x} = 0$ and W/a, where a forward difference and backward difference, respectively, were incorporated into our numerical scheme. The integrations in eqs 9 and 11 were then approximated by Simpson's method. In total, $M = (l_{max}+1)\times(2l_{max}+1)\times(N_x+1)$ variables need to be specified for the entire system of equations. We have found that Newton's method for solving nonlinear coupled equations converges fast in finding the roots of the resulting M coupled equations. The results in the next section are based on letting $l_{max} = 14$ and $N_x = 160$.

III. Results and Discussion

In a preliminary report of this work, we have shown the calculated phase diagram, Figure 2, where three phases, uniaxial, biaxial, and condensed, are stable in various parameter regimes.[40] These phases differ from each other by both the density variations across the slit and the orientational properties of the polymer segments in the slit, which will be analyzed in detail in the next two subsections.

For the density variation, below we consider

$$\tilde{\rho}(\tilde{x}) \equiv \int d\mathbf{u}\,\tilde{\rho}(\tilde{x},\mathbf{u}) \quad (20)$$

For the orientational properties, we define three separate measures along the principal axes with unit vectors $\hat{\mathbf{x}}$, $\hat{\mathbf{y}}$, and $\hat{\mathbf{z}}$,

$$S_\zeta(\tilde{x}) \equiv \frac{d\mathbf{u}\,P_2(u_\zeta)\tilde{\rho}(\tilde{x},\mathbf{u})}{\tilde{\rho}(\tilde{x})} \quad (21)$$

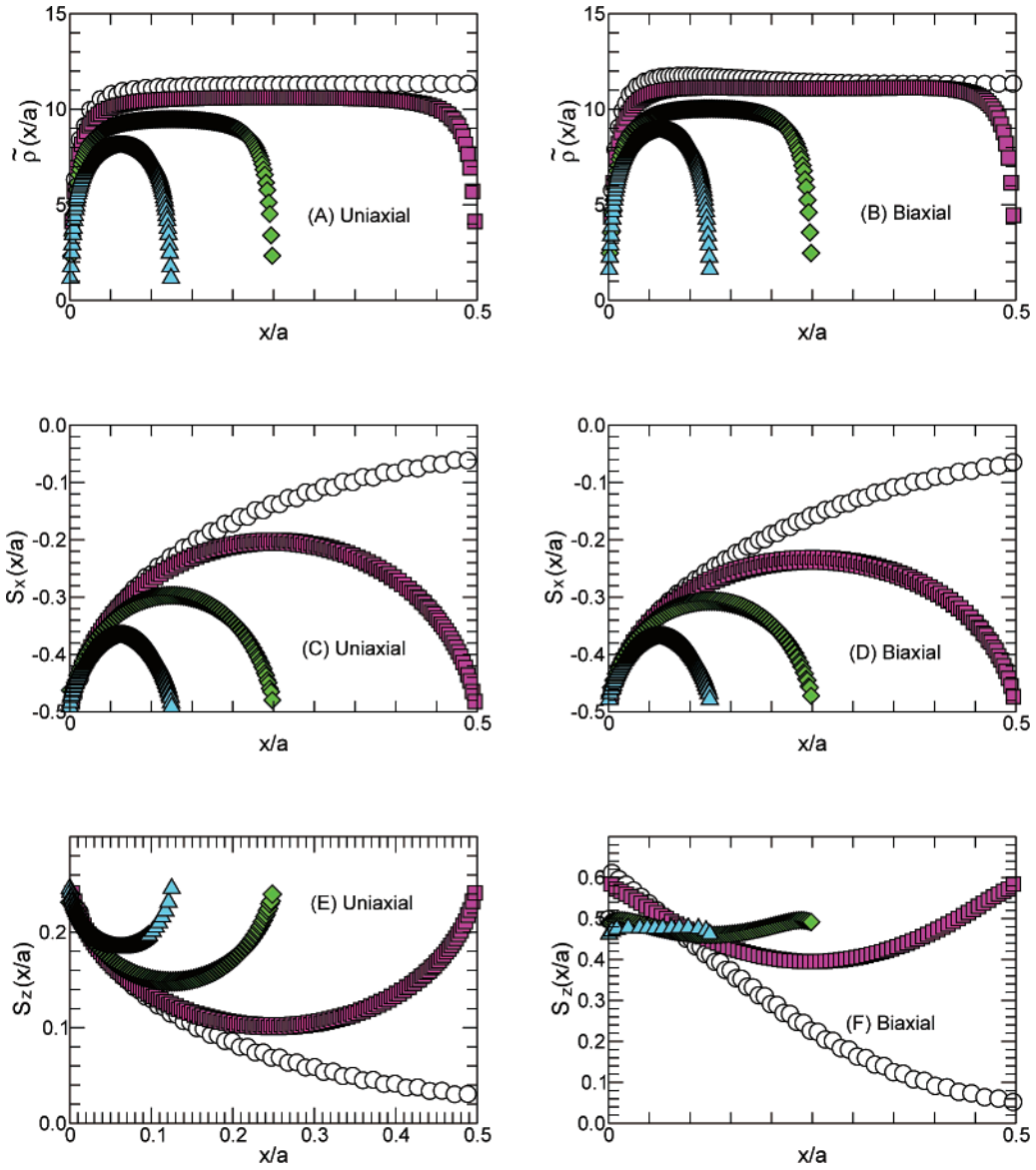

Figure 4. Density and order parameter profiles of the biaxial and uniaxial states for $W/a = 3$ (circles), 0.5 (squares), 0.25 (diamonds), and 0.125 (triangles) at the uniaxial-biaxial transition, corresponding to $\beta\mu = 17.92$, 17.10, 16.06, and 15.50, respectively. Only the portion near the left wall has been displayed for the $W/a = 3$ case.

where $\zeta = x, y, z$, and $u_x = \mathbf{u}\cdot\hat{\mathbf{x}}$, $u_y = \mathbf{u}\cdot\hat{\mathbf{y}}$ and $u_z = \mathbf{u}\cdot\hat{\mathbf{z}}$. Note that only two of these three functions are independent, since

$$S_x(\tilde{x}) + S_y(\tilde{x}) + S_z(\tilde{x}) \equiv 0 \tag{22}$$

The *uniaxial* (U) phase, for example, is characterized by

$$S_y(\tilde{x}) = S_z(\tilde{x}) = -S_x(\tilde{x})/2 \tag{23}$$

and the biaxial phase, by

$$S_y(\tilde{x}) \neq S_z(\tilde{x}) \tag{24}$$

Technically, the condensed phase is also biaxial, however, having a higher average density between the walls (see below). Here we have followed the terminology used in related studies[30,31] and refer to the low-density biaxial phase as a *biaxial* (B) phase and the high-density biaxial phase as a *condensed* (C) phase.

A. Uniaxial—Biaxial Transition. The physical properties of the current model are completely specified by the two basic parameters of the model described above, the reduced width of the slit W/a and the reduced chemical potential per segment $\beta\mu$. In the example experimental setup in Figure 1 $\beta\mu$ is directly related to the density $\tilde{\rho}_b$ of the bulk polymer solution [see eq 12]. In most parameter regimes considered below, the bulk solution is in the isotropic phase.

The uniaxial phase is stable in the low $\beta\mu$ region of the phase diagram in Figure 2. This region corresponds to a system where the excluded-volume interaction is relatively weak (low D/a) or the overall segmental density is relatively low. Examples of the reduced density variation $\rho(\tilde{x})$ are displayed in Figure 4A for various values of W/a and $\beta\mu$. Close to the wall, there exists a depletion layer of polymer segments. For large W/a, in the central region of the slit, the reduced density approaches the constant $\tilde{\rho}_b$ [see eq 12] and is independent of W/a.

One of the major physical features of the uniaxial phase is that the uniaxial symmetry of the orientational order parameters, reflected by eq 23, is maintained. Across the slit, the orientational structure can be characterized by a single order parameter, for example, $S_x(\tilde{x})$. The variation of the order parameters across the slit is shown in Figure 4, parts C and E, for several values of W/a and $\beta\mu$, where $S_x(0) \approx -1/2$, which is an indication of

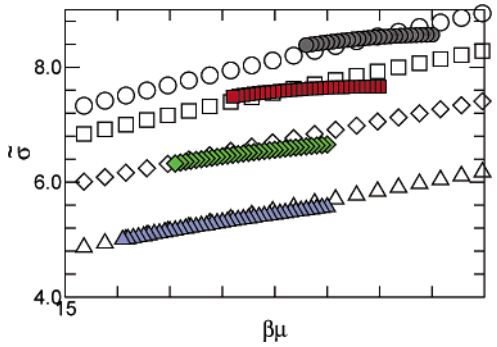

Figure 5. Reduced surface tension of the uniaxial (open symbols) and biaxial (filled symbols) phases for $W/a = 3$, 0.5, 0.25 and 0.125, represented by circles, squares, diamonds, and triangles, respectively.

a planar orientational distribution at the wall boundary. For large W/a, $S_x(\tilde{x})$ approaches 0 in the central region of the slit; coupled with the fact that the segmental density approaches ρ_b, the central region of the uniaxial phase has properties similar to those of the bulk isotropic phase with which it is in equilibrium.

For any value of W/a, Figure 2 shows that as $\beta\mu$ is increased to approach the solid curve associated with the circles in that figure, the system undergoes a phase transition to a biaxial phase having different orientational properties. Polymer segments far from the wall are still oriented nearly randomly and have a density similar to that in the uniaxial phase. For large W/a, however, polymer segments near the walls form thin layers of enhanced segmental density with nematic characteristics [Figure 4B]; a preferred direction parallel to the wall surface is spontaneously selected by the system as the local nematic director (defined as z in Figure 3). Orientational order parameters display typical biaxiality, $S_z(\tilde{x}) > |S_x(\tilde{x})|/2$. For the $W/a = 3$ case, the biaxiality is more profound within a surface layer of thickness approximately of order a [see Figure 4, parts D and F].

The U−B phase boundary in Figure 2 was numerically determined from calculation of the uniaxial and biaxial branches of the surface tension. Figure 5 shows four examples of the calculated $\tilde{\sigma}$ (eq 19) as a function of $\beta\mu$ for the uniaxial (open symbols) and biaxial (filled symbols) phases. The calculations were extended into the metastable regimes of both phases, and the crossing of the two branches defines the phase transition point. For $W/a = 3$ and 0.5, Figure 5 clearly shows that the two branches cross with different slopes, which is an indication of a first-order phase transition. For $W/a = 0.25$ and 0.125, the two branches are distinguished by small differences in slope at the transition point, characteristic of a weak first-order phase transition. Eventually, as $W/a \to 0$, the U−B transition becomes equivalent to the isotropic−nematic transition in two dimensions, where the phase transition in this model is second-order.[41] For $W/a \to \infty$, the U−B transition becomes equivalent to that found in a semi-infinite system with a single wall.[29]

Figure 6 shows the total reduced segmental density between the walls $\langle\tilde{\rho}\rangle W/a$ as a function of $\beta\mu$ for several values of W/a, where the average density

$$\langle\tilde{\rho}\rangle = \frac{a}{W}\int_0^{W/a} d\tilde{x}\, d\mathbf{u}\, \tilde{\rho}(\tilde{x},\mathbf{u}) \qquad (25)$$

The uniaxial and biaxial branches of $\langle\tilde{\rho}\rangle$ are represented by open and filled symbols, respectively. In both phases, the relationship between $\langle\tilde{\rho}\rangle$ and $\beta\mu$ is monotonic up to the uniaxial-biaxial transition point, where the curves undergo abrupt jumps.

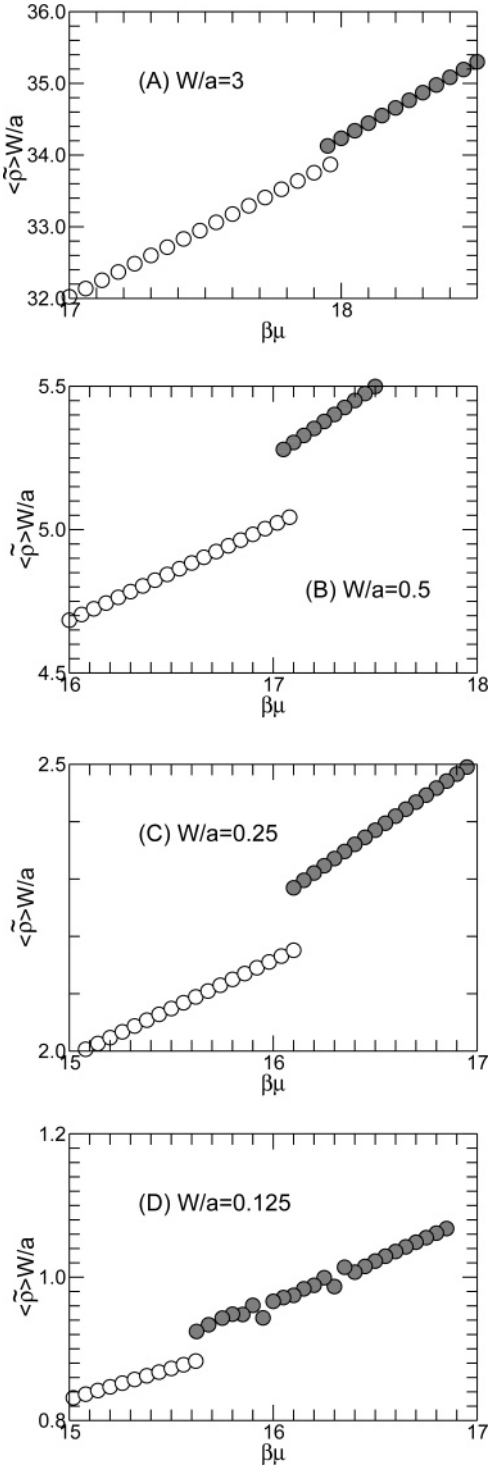

Figure 6. Reduced segmental density in the slit (see definition in eq 25) as a function of $\beta\mu$ for $W/a = 3$, 0.5, 0.25 and 0.125. The uniaxial and biaxial branches of this function are shown by using open and filled symbols, respectively.

Generally, for any W/a, increasing $\beta\mu$ is equivalent to increasing $\langle\tilde{\rho}\rangle$. As W/a increases, the magnitude of the discontinuity in the overall density, $\langle\tilde{\rho}\rangle W/a$, increases and approaches the excess number of segments per unit area of the biaxial phase over that of the uniaxial phase in a single-wall problem.

The first-order nature of the transition can also be seen in Figure 7, where the total biaxiality

$$\langle\Delta S\rangle = \int_0^{W/a} d\tilde{x}\, [S_z(\tilde{x}) - S_y(\tilde{x})] \qquad (26)$$

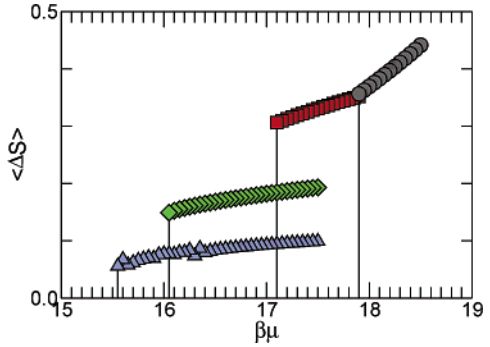

Figure 7. Average biaxiality as a function of $\beta\mu$ for $W/a = 3$, 0.5, 0.25 and 0.125.

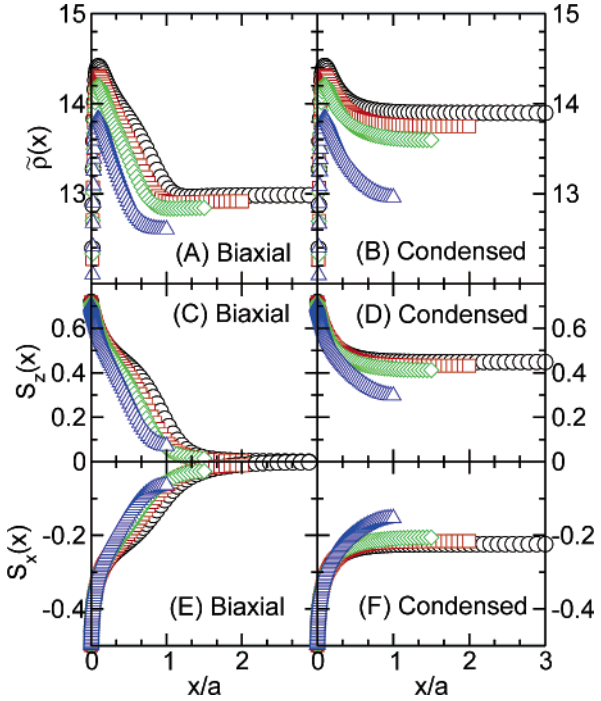

Figure 8. Density and order parameter profiles in the half space of the condensed and biaxial states for $W/a = 6$ (circles), 4 (squares), 3 (diamonds), and 2 (triangles) at the biaxial-condensed transition, corresponding to $\beta\mu = 20.4$, 20.3, 20.1, and 19.8 respectively.

is plotted as a function of $\beta\mu$. At the transition point, $\langle\Delta S\rangle$ undergoes an abrupt increase from 0 in the uniaxial phase to a nonzero value in the biaxial phase.

Studies of lyotropic rigid rods by van Roij et al.[30−32] using the Zwanzig model, have found the U−B transition to be second-order. Both first-order and second-order U−B transitions were predicted by Landau−de Gennes theories of thermotropic liquid crystals against a single wall.[26,42] At least within the current model, the U−B transition is first-order in most parameter regimes.

B. Biaxial-Condensed Transition. Returning to the phase diagram in Figure 2, one notes that there is another phase transition at a higher $\beta\mu$ for a fixed W/a ($\gtrsim$1.7). As $\beta\mu$ is raised above the uniaxial-biaxial transition boundary, the average reduced density $\langle\tilde{\rho}\rangle$ also increases. The density-enhanced layer near the wall broadens and develops stronger nematic characteristics; values of the local density near a wall may even exceed $\tilde{\rho}_N = 14.04$, the value in the nematic phase at the bulk isotropic−nematic (IN) transition. The biaxial phase remains stable as long as the reduced density far from the walls is still below the value of the isotropic phase of the bulk IN transition, $\tilde{\rho}_I = 13.05$ (corresponding to $\beta\mu_{IN} = 20.50$).[5,6]

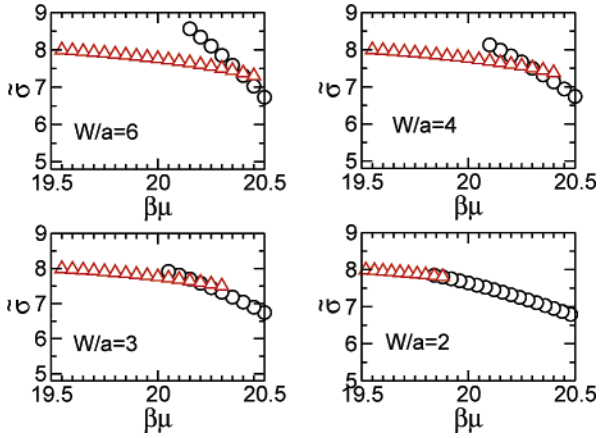

Figure 9. Reduced surface tension of the biaxial (triangles) and condensed (circles) phases as a function of the reduced chemical potential for $W/a = 6$, 4, 3 and 2.

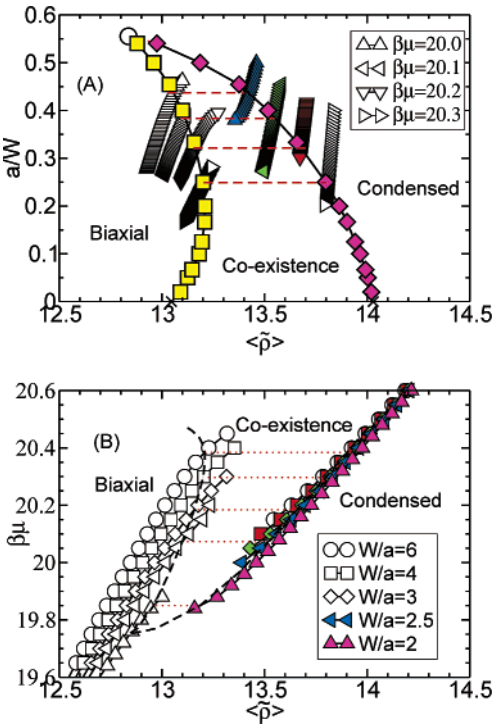

Figure 10. Phase diagrams showing the biaxial-condensed transition, plotted in terms of (A) a/W and $\langle\tilde{\rho}\rangle$ and (B) $\beta\mu$ and $\langle\tilde{\rho}\rangle$, where $\langle\tilde{\rho}\rangle$ is the average density within the slit, eq 25. In plot A, the lines associated with squares and diamonds are the phase boundaries, inside which both biaxial and condensed phases coexist. In plot B, the phase boundaries are represented by the dashed curves. Furthermore, we have shown the two branches of the function $a/W(\langle\tilde{\rho}\rangle,\beta\mu)$ for given $\beta\mu$ using triangles in plot A, and the function $\beta\mu(\langle\tilde{\rho}\rangle,W/a)$ for given W/a using various symbols in plot B. The crosses in part A for $a/W = 0$ represent the isotropic and nematic transition densities of the bulk system.

As $\beta\mu$ approaches the biaxial-condensed phase boundary, one of the distinctive features of the biaxial density profile is that the thickness of the density-enhanced surface layer expands beyond a and develops into a thick partial wetting layer (see Figure 8). For very large W/a, this expansion of the biaxial layers continues until $\beta\mu$ reaches $\beta\mu_{IN}$, where the thickness of the wetting layer diverges, which results in complete wetting by the nematic phase at a single wall.[29] For smaller W/a, however, the dense wetting layers extending from both walls tend to merge, resulting in a new (*capillary) condensed* (or capillary nematized) phase, which becomes stable after $\beta\mu$ reaches the solid-phase boundary associated with the squares in Figure 2.

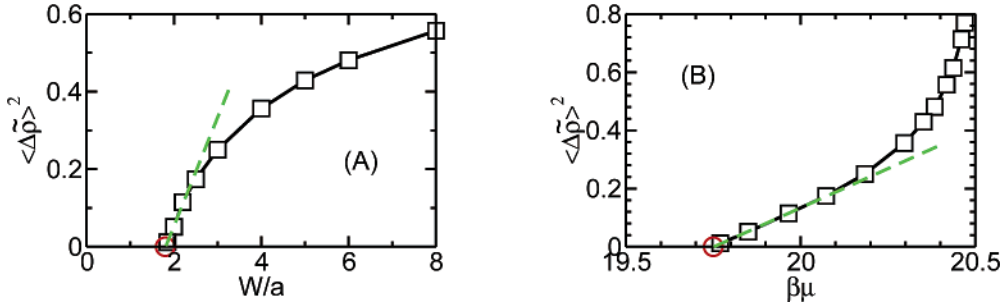

Figure 11. Squared density difference $\langle\Delta\tilde{\rho}\rangle^2$ at the biaxial-condensed phase transition as a function of (A) W/a and (B) $\beta\mu$. The open circles represent the estimated critical point.

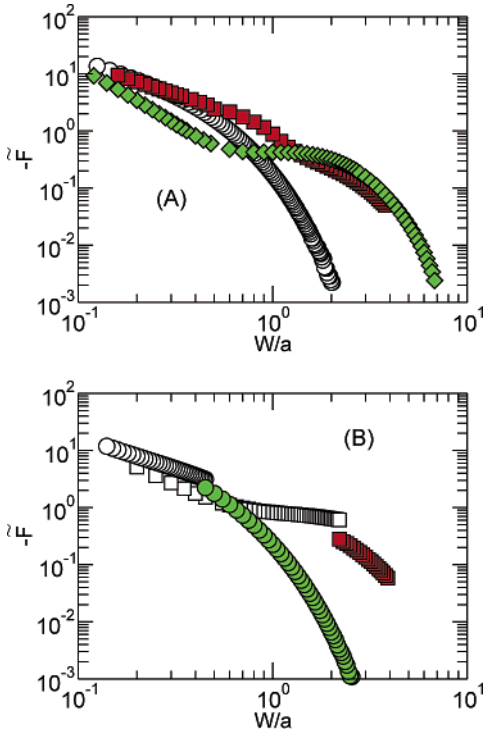

Figure 12. Magnitude of the induced attraction between the two walls as a function of W/a in five cases: $\beta\mu = 14$ [circles in A], 17 [circles in B], 18 [squares in A], 20 [squares in B], and 21.5 [diamonds in A].

At this phase transition, the average density in the slit jumps to a value comparable to $\tilde{\rho}_N$. Orientational order parameters still display typical biaxiality, i.e., $S_z(\tilde{x}) > |S_x(\tilde{x})|/2$, but the order parameter S_z near the center of the slit grows and approximately reaches the asymptotic value $S_z = 0.4618$ of the nematic phase at the bulk isotropic−nematic transition.[5,6] For $W/a \to \infty$, this biaxial-condensed transition becomes the bulk I−N transition.

To study the characteristics of the biaxial-condensed transition, in Figure 9 we examine the two branches of the surface tension as a function of the reduced chemical potential $\beta\mu$ for a few values of W/a. In this figure, the biaxial branch (triangles) crosses the condensed branch (circles) with a different slope, indicating that the transition is first-order. Note that the slopes of the crossing lines at the transition approach each other as W/a is lowered; this is a reflection of the fact that the first-order nature of the biaxial-condensed transition becomes weaker as W/a decreases.

The biaxial-condensed phase transition, however, does not exist for a sufficiently narrow slit with $W/a \gtrsim 1.7$. Because of the limited space between the walls, the system does not support the adequate development of the condensed state, which typically requires a partial wetting layer of the width a. The transition between the biaxial and condensed phases is now continuous without any signature of a phase transition [Figure 2]. The first-order phase boundary between the biaxial and condensed phases terminates at a critical point W_c/a and $\beta\mu_c$.

Although we have described the biaxial-condensed transition using W/a and $\beta\mu$ as independent variables, the same transition can be viewed in other representations.[30,31] Figure 10A shows the phase diagram in an $a/W-\langle\tilde{\rho}\rangle$ graph, where we have also plotted the function $a/W(\langle\tilde{\rho}\rangle,\beta\mu)$ for the biaxial and condensed branches for given $\beta\mu$. The plots, based on our numerical solution, have been extended into the coexistence region. The circle in the figure represents the critical point, where the coexistence region vanishes. An additional perspective can be gained from the phase diagram plotted in terms of $\beta\mu$ and $\langle\tilde{\rho}\rangle$ shown in Figure 10B. The two branches of the function $\beta\mu(\langle\tilde{\rho}\rangle,W/a)$ for several values of W/a have also been plotted in this diagram. As $\beta\mu$ is lowered, the difference between the coexisting densities decreases, terminating at the critical point.

In order to more precisely determine the critical point (the location of the filled square in Figure 2) specified by μ_c and W_c, we have considered the difference $\langle\Delta\tilde{\rho}\rangle$ of the coexisting densities, represented by the magnitude of the dashed lines in Figure 10A and the dotted lines in Figure 10B. Since we are dealing with a mean-field theory, we expect

$$\langle\Delta\tilde{\rho}\rangle \propto (W - W_c)^{1/2} \tag{27}$$

for Figure 10A, and

$$\langle\Delta\tilde{\rho}\rangle \propto (\mu - \mu_c)^{1/2} \tag{28}$$

for Figure 10B.

Hence, plots of $\langle\Delta\tilde{\rho}\rangle^2$ as a function of W/a from Figure 10A and of $\langle\Delta\tilde{\rho}\rangle^2$ as a function of $\beta\mu$ from Figure 10B should follow straight lines near the critical point; the intercepts from such plots, shown in Figure 11, give us

$$W_c/a = 1.7 \pm 0.1 \tag{29}$$

$$\beta\mu_c = 19.2 \pm 0.3 \tag{30}$$

for the present model.

C. Suggested Experiment. Returning to the experimental setup in Figure 1, we see that the chemical potential of the entire system, hence μ inside the slit, can be controlled by the segmental density of wormlike chains in the bulk. In general, in all three confined phases at a constant μ, a narrower slit

produces stronger nematic characteristics. The excess free energy as a function of W/a at constant $\beta\mu$, eq 11, decreases as W/a decreases. This reduction induces an *attraction* between the illustrated plates in Figure 1, mediated by the repulsive Onsager excluded volume interaction between wormlike chains in the slit.

Using a finite difference method, we have computed this (disjoining) force F according to the definition[43]

$$\tilde{F} \equiv a^2 D\beta F = -\frac{\partial\tilde{\sigma}(W/a,\beta\mu)}{\partial(W/a)} \tag{31}$$

for a few typical values of $\beta\mu$ and plotted the results in Figure 12. In Figure 12A, $\tilde{F}$ is a continuous function of W/a for all three cases, $\beta\mu = 14$ (circles), 18 (squares) or 21.5 (diamonds), where the system is in the uniaxial, biaxial or condensed phases, respectively. The attraction between the plates is short-ranged and is significant only when the slit width W is comparable to the Kuhn length a.

In Figure 12B, $\tilde{F}$ is a discontinuous function of W/a for both $\beta\mu = 17$ (circles) and 20 (squares), where the system undergoes a first-order phase transition as W/a changes, uniaxial−biaxial in the first case and biaxial-condensed in the second case. An experimental setup that detects these discontinuities in the induced attraction between the plates would directly probe the phase boundaries determined in this work.

Although flat surfaces have been used in the current model for conceptualization, we would expect that curved surfaces can produce similar type of attractions as well, so long as the reciprocal curvatures of the surfaces are greater than the Kuhn length of wormlike chains in the solvent. The detection of the induced capillary force between flat and spherical surfaces immersed in a liquid-crystalline medium is probably more practical to realize experimentally and has been performed on a number of nonpolymeric systems.[44−46] These experiments have probed the capillary forces induced by near-surface liquid crystal enhancements while the bulk phase is still in its isotropic state, although the nature and cause of the surface enhancements are not exactly the same as in the current model. A theoretical calculation based on the Landau−de Gennes theory of a slit system has also indicated that the force−distance curve would display a discontinuity above the isotropic−nematic transition,[47] similar to the curve represented by circles in Figure 12B. We stress that in our model, the attraction between the plates is completely induced by excluded-volume repulsions between the wormlike polymer chains.

As a final remark in this subsection, for conceptual illustration we proposed a possible experiment on the basis of detecting capillary force; other experimental techniques, including exploiting the optical properties of various phases, might also be designed to detect the phase transitions.

IV. Summary

In summary, the confinement of wormlike polymer chains was studied with the inclusion of the Onsager excluded-volume interaction. We have also shown that three distinct phases, uniaxial, biaxial, and condensed, may exist in this system, depending on the magnitude of the slit width and average density within the slit.

The computation in this work focuses on the phase behavior by employing a ground-state dominance approximation that ignores the path ($t-$) dependence of the probability distribution function [see eqs 4 and 5]. In semiflexible polymer liquid crystals, polymers make hairpin turns to accommodate the orientational ordering,[4,5,48−50] This and other conformational properties can be explored by using the current formalism and the results for the mean field, after the incorporation of the $t-$dependence in the differential equation,[49] eq 4. This is beyond the scope of the current work.

Appendix

A. List of Constants. For the coefficients used in eq 16

$$d_l = \begin{cases} \pi/4 & l = 0, \\ 0, & l = 1, 3, 5, ..., \\ -\dfrac{\pi(2l+1)l!(l-2)!}{2^{2l+1}\left(\frac{l}{2}-1\right)!\left(\frac{l}{2}\right)!\left(\frac{l}{2}\right)!\left(\frac{l}{2}+1\right)!} & l = 2, 4, 6, ... \end{cases} \tag{32}$$

For the coefficients in eqs 15 and 18

$$I_{l_1,m_1,l_2,m_2,l_3,m_3} = \int \mathrm{d}\mathbf{u}\, Y_{l_1,m_1}(\theta,\phi) Y_{l_2,m_2}(\theta,\phi) Y_{l_3,m_3}(\theta,\phi) \tag{33}$$

Acknowledgment. We wish to acknowledge NSERC for financial support and SHARCNET for computation time.

References and Notes

(1) Khokhlov, A. R.; Semenov, A. N. *Physica* **1982**, *112A*, 605.
(2) Onsager, L. *Ann. N.Y. Acad. Sci.* **1949**, *51*, 627.
(3) Vroege, G. J.; Lekkerkerker, H. N. W. *Rep. Prog. Phys.* **1992**, *55*, 1241.
(4) Odijk, T. *Macromolecules* **1986**, *19*, 2313.
(5) Vroege, G. J.; Odijk, T. *Macromolecules* **1988**, *21*, 2848.
(6) Chen, Z. Y. *Macromolecules* **1993**, *26*, 3419.
(7) Wessels, P. P. F.; Mulder, B. M. *Soft Mater.* **2003**, *1*, 313.
(8) Jaffer, K. M.; Opps, S. B.; Sullivan, D. E.; Nickel, B.; Mederos, L. *J. Chem. Phys.* **2001**, *114*, 3314.
(9) Pickett, G. T.; Schweizer, K. S. *J. Chem. Phys.* **1999**, *110*, 6597.
(10) Hino, T.; Prausnitz, J. M. *Polymer* **1999**, *40*, 1241.
(11) Purday, K. R.; Fraden, S. *Phys. Rev. E* **2004**, *70*, 061703.
(12) Herzfeld, J. *J. Mol. Rec.* **2004**, *17*, 376.
(13) Dong, Y.; Wu, Y.; Wang, J.; Wang, M. *Eur. Polym. J.* **2001**, *37*, 1713.
(14) Dong, Y.; Wang, H.; Zheng, W.; Zhao, Y.; Bi, D.; Zhao, L.; Li, X. *Carbohydr. Polym.* **2004**, *57*, 235.
(15) Zweckstetter, M.; Bax, A. *J. Biomol. NMR* **2001**, *20*, 365.
(16) Fraden, S.; Maret, G.; Caspar, D. L. D. *Phys. Rev. E* **1993**, *48*, 2816.
(17) Chen, W. L.; Sato, T.; Teramoto, A. *Macromolecules* **1998**, *31*, 6506.
(18) Kassapidou, K.; Jesse, W.; van Dijk, J. A. P. P.; van der Maarel, J. R. C. *Biopolym.* **1998**, *46*, 31.
(19) Tang, J. X.; Fraden, S. *Liq. Cryst.* **1995**, *19*, 459.
(20) Lu, X. J.; Kindt, J. T. *J. Chem. Phys.* **2004**, *120*, 10328.
(21) Yethiraj, A.; Fynewever, H. *Mol. Phys.* **1998**, *93*, 693.
(22) Fynewever, H.; Yethiraj, A. *J. Chem. Phys.* **1998**, *108*, 1636.
(23) Dijkstra, M.; Frenkel, D. *Phys. Rev. E* **1995**, *51*, 5891.
(24) Sheng, P. *Phys. Rev. Lett.* **1976**, *37*, 1059.
(25) Sheng, P. *Phys. Rev. A* **1982**, *26*, 1610.
(26) Sluckin, T. J.; Poniewierski, A. *Phys. Rev. Lett.* **1985**, *55*, 2907.
(27) Sen, A. K.; Sullivan, D. E. *Phys. Rev. A* **1987**, *35*, 1391.
(28) Cui, S. M.; Akcakir, O.; Chen, Z. Y. *Phys. Rev. E* **1995**, *51*, 4548.
(29) Chen, Z. Y.; Cui, S. M. *Phys. Rev. E* **1995**, *52*, 3876.
(30) van Roij, R.; Dijkstra, M.; Evans, R. *Europhys. Lett.* **2000**, *49*, 350.
(31) van Roij, R.; Dijkstra, M.; Evans, R. *J. Chem. Phys.* **2000**, *113*, 7689.
(32) Dijkstra, M.; van Roij, R.; Evans, R. *Phys. Rev. E* **2001**, *63*, 051703.
(33) Zwanzig, R. *J. Chem. Phys.* **1963**, *39*, 1714.
(34) Freed, K. F. *Adv. Chem. Phys.* **1972**, *22*, 1.
(35) Chen, J. Z. Y.; Sullivan, D. E. *Macromolecules* **2006**, *39*, 7769.
(36) Casassa, E. F.; Tagami, Y. *Macromolecules* **1969**, *2*, 14.
(37) Doi, M.; Edwards, S. F. *The theory of polymer dynamics*; Oxford University Press: New York, 1988.
(38) Odijk, T. *Macromolecules* **1983**, *16*, 1340.
(39) Burkhardt, T. W. *J. Phys. A: Math Gen.* **1997**, *30*, L167.
(40) Chen, J. Z. Y.; Yuan, X.; Sullivan, D. E. *Europhys. Lett.* **2005**, *72*, 89.
(41) Chen, Z. Y. *Phys. Rev. Lett.* **1993**, *71*, 93.
(42) Seidin, R.; Hornreich, R. M.; Allender, D. W. *Phys. Rev. E* **1997**, *55*, 4302.
(43) Poniewierski, A.; Sluckin, T. J. *Liq. Cryst.* **1987**, *2*, 281.

(44) Kočevar, K.; Borštnik, A.; Muševič, I.; Žumer, S. *Phys. Rev. Lett.* **2001**, *86*, 5914.
(45) Borštnik Bračič, A.; Kočevar, K.; Muševič, I.; Žumer, S. *Phys. Rev. E.* **2003**, *68*, 011708.
(46) Shinto, H.; Kobayashi, K.; Hyodo, T.; Ishiba, N.; Higashitani, K. *Chem. Lett.* **2005**, *34*, 1318.
(47) Borštnik, A.; Žumer, S. *Phys. Rev. E* **1997**, *56*, 3021.
(48) Tkachenko, A.; Rabin, Y. *Macromolecules* **1995**, *28*, 8646.
(49) Odijk, T. *J. Chem. Phys.* **1996**, *105*, 1270.
(50) Spakowitz, A. J.; Wang, Z.-G. *J. Chem. Phys.* **2003**, *119*, 13113.

MA062160M